POAC'13
Espoo, Finland

Proceedings of the 22nd International Conference on
Port and Ocean Engineering under Arctic Conditions
June 9-13, 2013
Espoo, Finland

POLARIMETRIC DECOMPOSITION ANALYSIS OF SEA ICE DATA

Torbjørn Eltoft[1,3], **Anthony P. Doulgeris**[1], **Sebastian Gerland**[2], **and Mari-Ann Moen**[1]

[1]*University of Tromsø, The Auroral Observatory, 9037 Tromsø, Norway.*
[2]*Norwegian Polar Institute, FRAM centre, 9296 Tromsø, Norway*
[3]*Northern Research Institute, Norway*

ABSTRACT

This paper presents a strategy for analyzing polarimetic SAR images of Arctic sea ice. The analysis is exemplified using a quad-pol C-band SAR image collected by the Canadian satellite Radarsat-2 over an area north of Svalbard in April 2011. Our analysis approach is conducted in several steps. Initially, the SAR image is segmented into distinct classes using an unsupervised classification algorithm, which incorporates both polarimetric and statistical signal features. In the second step, the image segments are analyzed in terms of polarimetric properties to infer information about ice properties. We show examples of some polarimetric features which clearly contain important sea information.

1. *INTRODUCTION*

Radar signatures of sea ice are typically complex, and require careful analysis to enable the extraction of useful and accurate surface information. The interpretation of SAR-derived signatures therefore requires a thorough understanding of the interaction of electromagnetic radiation with the snow and ice layers, and of how this interaction depends on both surface properties (e.g. roughness, salinity), and imaging parameters(frequency, incidence angle, and polarization).

The backscattered radar signals from sea ice will generally be a result of a combination of several scattering mechanisms. The relative contributions of rough surface scattering, specular reflections, volume scattering and multiple scattering processes depend on thickness, degree of deformation, size of deformed structures, amount of snow on the ice, salinity and compactness of the ice fragments [1]. Full polarimetric SAR (polSAR) observations allow for decomposition of the signals into components representing the contributions from the various scattering mechanisms.

This paper presents the study of a full polarization (quad-pol) SAR scene of Arctic sea ice collected north of Svalbard in April 2011. In addition to the SAR scene, we have available ground truth data collected along helicopter tracks in the area and at point stations on the ice. The analysis is performed in several steps. Initially, the SAR image is segmented into distinct classes using an unsupervised classification algorithm, which incorporates both polarimetric and statistical signal features. The resulting classes are thus distinguished by differences in statistical and polarimetric properties, but they are unlabeled with respect to ice types. In the second step, a model-based polarimetric decomposition is applied to the PolSAR image to identify the dominant scattering mechanisms. In the final stage, the segmented image is used to mask out image areas associated with the various segments, and each segment is characterized in terms of their polarimetric properties. To help validate the satellite based

sea ice information, the image segments are also manually analyzed by sea ice experts, which are based on the SAR data and all available in-situ information, and give their opinion about ice type and ice properties.

The paper is organized as follows. Section 2 gives some preliminaries on the physics of sea ice. In section 3 gives some preliminaries on SAR polarimetry. The segmentation and decomposition algorithms are discussed in section 4. Section 5 describes the data, and section 6 summarizes the results of the analysis is presented. Finally, section 7 gives some conclusions.

2. *SEA ICE PRELIMINARIES*

The appearance of sea ice in a SAR image is determined by the interaction between the electromagnetic (EM) field and the ice, and is strongly related to the properties of the surface and the medium directly below the surface. Sea ice is an inhomogeneous medium composed of an ice background, brine inclusions, air bubbles, and solid salt [2]. The electromagnetic properties of these constituents are characterized by permeabilities and permittivities, which relate material characteristics to electromagnetic fields by constitutive relations [3]. Sea ice is basically non-magnetic, and EM wave propagation is given by the dielectric properties. The effective permittivity of sea ice is determined by how ice, brine, air bubbles, and solid salt are mixed. Inhomogeneities in the ice are responsible for both wave attenuation and scattering.

Sea ice can be divided into two major categories, first-year ice (FY) and multi-year ice (MY). MY-ice has survived at least one summer melt and is discriminated from FY-ice on the basis of properties such as deformation (roughness, surface topography), thickness, salinity and snow cover. Because of winds and currents the Arctic ice pack is kept in almost continuous motion, resulting in significant deformation (i.e. ridging) of the ice. The extent of deformation is exploited when trying to discriminate ice types. The most commonly referred sea ice types are level ice, rafted ice, ridged ice, rubble fields and hummocked ice. Level ice is ice with a relatively flat surface, which has not been deformed to any extent. Rafted ice arises when ice sheets collide and override one another, it occurs usually on new and FY-ice. Pressure processes cause the ice to pile up both above and below the surface. A ridge is the result of such processes and can be described as a long line of piled up, cracked ice. Repeated ridging causes rubble fields. Leads are open water channels in areas of predominantly sea ice. In addition to deformation characteristics there exist several ice types representing young and thin sea ice.

In respect to SAR imaging, surface roughness is defined relative to the wavelength, and X-, C- and L-band images (corresponding to the frequencies around 10, 5, and 1 GHz, respectively) will image identical surfaces differently. The backscattered signals from sea ice result from a combination of several scattering mechanisms. The relative contributions of rough surface scattering, specular reflections, volume scattering and multiple scattering processes depend on thickness, degree of deformation, size of deformed structures, amount of snow on the ice, salinity and compactness of the ice fragments [1].

3. *RADAR POLARIMETRY PRELIMINARIES*

Radar polarimetry is an advancing technology, which is getting increasing attention in various application areas of radar remote sensing. Polarimetry deals with the full vector nature of electromagnetic waves. General introductory texts on radar and SAR polarimetry are found in e.g. [4, 5, 6]. When there are changes in the index of refraction, as a consequence of changes in permittivity, magnetic permeability, or conductivity, the polarization state of an electromagnetic wave is transformed, and the

electromagnetic vector wave is re-polarized. When the wave passes through a medium of changing index of refraction, or when it strikes an object or a scattering surface and it is reflected, the characteristic information about the reflectivity, shape and orientation of the reflecting body can be obtained by polarimetric analysis of the echoes [6]. This information is only available if the radar system has full polarimetric capability. For the linear polarization basis, this means the system is able to measure the backscattered signal in four polarization channels. This is mathematically formulated by means of the Sinclair matrix (also referred to as the scattering matrix), which relates the backscattered wave vector to the incident wave vector, as shown in (1) below

$$\begin{bmatrix} E_h^s \\ E_v^s \end{bmatrix} = \frac{\exp(jkr)}{r} \begin{bmatrix} S_{HH} & S_{HV} \\ S_{VV} & S_{VH} \end{bmatrix} \begin{bmatrix} E_h^i \\ E_v^i, \end{bmatrix} \tag{1}$$

where k is wavenumber of the incident electromagnetic wave, r is the distance between the radar antenna and target, E_j^i and E_j^s, $j \in \{h, v\}$, denote the jth linear polarization component of the incident and scattered waves, respectively, and the entries of the S-matrix, i.e. S_{HH}, S_{HV}, S_{VV}, S_{VH}, define the channel wise complex scattering coefficients. For practical analysis of polarimetric data, the S-matrix is often vectorized; either as a lexicographic *scattering or target vector*

$$\mathbf{s} = [S_{HH}, S_{HV}, S_{VH}, S_{VV}], \tag{2}$$

or as a *Pauli scattering vector*

$$\mathbf{k} = \frac{1}{\sqrt{2}}[S_{HH} + S_{VV}, S_{HH} - S_{VV}, S_{HV} + S_{VH}, j\,(S_{HV} - S_{VH})], \tag{3}$$

where the square-root factor maintains the total backscattered power. Data in this format is denoted single look complex (SLC) data. A scattering mechanism is often defined as a normalized Pauli scattering vector, because this can be used to characterize differences in polarized wave scattering [5].

Multi-looking the $\mathbf{s}$ or $\mathbf{k}$ vectors results in the *polarimetric covariance matrix* or *coherence matrix*, defined as

$$\mathbf{C} =< \mathbf{s}\mathbf{s}^\dagger >= \frac{1}{L}\sum_{i=1}^{L} \mathbf{s}_i\mathbf{s}_i^\dagger \text{ and } \mathbf{T} =< \mathbf{k}\mathbf{k}^\dagger >= \frac{1}{L}\sum_{i=1}^{L} \mathbf{k}_i\mathbf{k}_i^\dagger, \tag{4}$$

respectively, where the superscript † refers to conjugate transpose, and L is the nominal number of looks. This data format is called multi-looked complex (MLC) data.

A sea ice surface is generally considered to fulfill the requirement of *reciprocity*, i.e. $S_{HV} = S_{VH}$. In the remainder, we will also assume *reflection symmetry*, in which case the $\mathbf{C}$ and $\mathbf{T}$ matrices take the following forms:

$$\mathbf{C} = \begin{bmatrix} C_{11} & 0 & C_{13} \\ 0 & C_{22} & 0 \\ C_{13}^* & 0 & C_{33} \end{bmatrix} \text{ and } \mathbf{T} = \begin{bmatrix} T_{11} & T_{12} & 0 \\ T_{12}^* & T_{22} & 0 \\ 0 & 0 & T_{33} \end{bmatrix} \tag{5}$$

3.1. Some polarimetric parameters

In the following we briefly introduce some polarimetric parameters which have previously been shown to convey sea ice information.

Co-polarization ratio: The co-polarization ratio is defined as the ratio between the received HH-power and the received VV-power.

$$R_{hh/vv} = \frac{< S_{HH} S_{HH}^{\dagger} >}{< S_{VV} S_{VV}^{\dagger} >} = \frac{C_{11}}{C_{33}} = \frac{T_{11} + T_{12} + T_{21} + T_{22}}{T_{11} - T_{12} - T_{21} + T_{22}}. \tag{6}$$

In the simple Bragg-scattering model (small perturbation model), the surface roughness spectrum appears as a multiplicative factor in the expression for the backscattered intensity [7]. Hence, the effect of roughness will be cancelled out in the ratio of like polarization channels. The co-polarization ratio will be a function of the dielectric constant, as well as of the incidence angles.

The phase difference between HH and VV has been reported to be related to ice thickness, especially for thin ice [8].

Scattering entropy and anisotropy: Let the $\mathbf{T}$ matrix be decomposed into eigenvalues and vectors as

$$\mathbf{T} = \lambda_1 \mathbf{e}_1 \mathbf{e}_1^{\dagger} + \lambda_2 \mathbf{e}_2 \mathbf{e}_2^{\dagger} + \lambda_3 \mathbf{e}_3 \mathbf{e}_3^{\dagger}, \tag{7}$$

where $\mathbf{e}_i,\ i = \{1, 2, 3\}$ are eigenvectors, and $\lambda_1 > \lambda_2 > \lambda_3$ are the corresponding eigenvalues. The scattering entropy H is an indicator of randomness in scattering mechanisms and is derived from the eigenvalues of $\mathbf{T}$ as

$$H = -\sum_{i=1}^{3} P_i log_3(P_i), \tag{8}$$

where $P_i = \frac{\lambda_i}{\sum_{j=1}^{3} \lambda_j}$.

The polarimetric anisotropy A measures the imbalance between the second and third eigenvalues, and is defined by

$$A = \frac{P_2 - P_3}{P_2 + P_3}. \tag{9}$$

Circular RR/LL-coherence: The magnitude and phase of the coherence between the circular RR and LL polarizations can be calculated from the $\mathbf{T}$-matrix as [9]

$$\rho_{RR/LL} = \left| \frac{T_{22} - T_{33} + j(T_{23} + T_{32})}{T_{22} + T_{33}} \right|, \tag{10}$$

and

$$\phi_{RR/LL} = tan^{-1} \left(\frac{-Re\{T_{23} + T_{32}\}}{T_{33} - T_{22} + Im\{T_{23} + T_{32}\}} \right), \tag{11}$$

where $Re\{\cdot\}$ and $Im\{\cdot\}$ denote the real part and imaginary part of the expressions. The polarimetric coherence between RR and LL has been found to be sensitive the surface roughness in [10]. It is noted that under the assumption of reflection symmetry, the phase term is alway zero.

4. *METHODS*

Fig.1 gives a general workflow for the retrieval of sea ice information from a multi-polarization SAR image. The first step is a unsupervised segmentation of the image, which subdivides it into a given number of segments based on variations in statistical and polarimetric properties. This step is followed by a polarimetric analysis, where the objective is to infer the polarimetric properties of each image segment. These properties may be interpreted in terms of physical characteristics, which may help

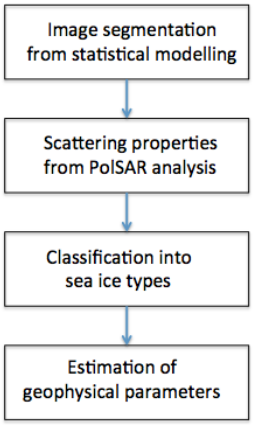

Figure 1. General workflow for sea ice information retrieval from PolSAR data.

label the segments as ice types. The final step includes estimating geophysical properties e.g. ice thickness or ice concentration. Here, we mostly address the first two steps.

PolSAR image segmentation

The segmentation algorithm uses the following 6 parameters generated from the general (3×3) **C**-matrix associated with the scattering vector $\mathbf{s} = [S_{HH}, \frac{1}{\sqrt{2}}(S_{HV} + S_{VH}), S_{VV}]$, [11].

Relative kurtosis is a measure of non-Gaussianity, and is calculated from SLC and MLC data as described in Eq.(12):

$$RK = \frac{1}{Ld(d+1)} \sum_{i=1}^{L} \left[\mathbf{s}_i^{\dagger} \mathbf{C}^{-1} \mathbf{s}_i \right]^2. \tag{12}$$

In Eq.(12) L is the number of multi-looks and d is the dimension of the scattering vector $\mathbf{s}$. All the other parameters are calculated from MLC data.

Geometric brightness represents the total intensity, i.e. it is a measure of the combined channel intensities:

$$B = \sqrt[d]{det(\mathbf{C})}. \tag{13}$$

Co-polarization ratio:

$$R_{HH/VV} = \frac{\langle S_{HH} S_{HH}^* \rangle}{\langle S_{VV} S_{VV}^* \rangle}. \tag{14}$$

Cross-polarization ratio:

$$R_{HV/B} = \frac{\langle S_{HV} S_{HV}^* \rangle}{B}. \tag{15}$$

Co-polarization correlation magnitude:

$$|\rho| = \left| \frac{\langle S_{HH} S_{VV}^* \rangle}{\sqrt{\langle S_{HH} S_{HH}^* \rangle \langle S_{VV} S_{VV}^* \rangle}} \right|. \tag{16}$$

Co-polarization correlation angle:

$$\angle\rho = \angle(\langle S_{HH} S_{VV}^* \rangle). \tag{17}$$

These six features are non-linearly transformed such that the marginal probability density functions (pdfs) have a Gaussian-like appearance at the peaks. We then model the global pdf as a multivariate

Gaussian mixture distribution, and segment the image into a given number of unlabeled segments using the expectation maximition algorithm, as described in [11]. The features were transformed as follows; we use the reciprocal of the relative kurtosis; the next three were logarithmically transformed; the last two were not transformed at all. The number of classes input to the algorithm was manually estimated based on optical images, the Pauli image, the sea ice observation log, and the segmentation results obtained with different number of classes.

Polarimetric decomposition

In the 3-dimensional Pauli representation, the scattering vector is, under the reciprocity assumption, defined as

$$\mathbf{k}_P = \frac{1}{\sqrt{2}}[s_{hh} + s_{vv}, s_{hh} - s_{vv}, 2s_{hv}], \tag{18}$$

where the square-root factor is used to keep the total backscattered power constant. In the corresponding multilook PolSAR image, each pixel is represented by a (3×3) coherency matrix T, which is a non-negative definite, Hermitian matrix. If we additionally assume reflection symmetry, the coherence matrix will be of the form of equation (5). The Freeman-Durden decomposition [12] has been successfully applied to analyze polarimetric data of forest. The decomposition models the coherency matrix as the contribution of three scattering mechanisms: surface, double-bounce, and volume scattering, i.e.

$$\mathbf{T} = P_s\,\mathbf{T}_s + P_d\,\mathbf{T}_d + P_v\,\mathbf{T}_v, \tag{19}$$

where

$$\mathbf{T}_s = \frac{1}{1+|\beta|^2}\begin{bmatrix} 1 & \beta & 0 \\ \beta^* & |\beta|^* & 0 \\ 0 & 0 & 0 \end{bmatrix}, \tag{20}$$

$$\mathbf{T}_d = \frac{1}{1+|\alpha|^2}\begin{bmatrix} |\alpha|^* & \alpha & 0 \\ \alpha^* & |\alpha|^* & 0 \\ 0 & 0 & 0 \end{bmatrix}, \tag{21}$$

$$\mathbf{T}_v = \frac{1}{4}\begin{bmatrix} 2 & 0 & 0 \\ 0 & 1 & 0 \\ 0 & 0 & 1 \end{bmatrix}. \tag{22}$$

The Freeman-Durden method sometimes produces non-physical solutions for P_s and P_d. To avoid this, we apply a modified form, in which we only remove a fraction of the volume component, i.e., we define $\mathbf{T}_g = \mathbf{T} - a\mathbf{T}_v$, where the multiplying factor a secures that the eigenvalues of $\mathbf{T}_g$ is positive. The decomposition then follows the standard Freeman-Durden decomposition as depicted in Fig.2. We will refer to this decomposition approach as the non-negative definite (NNED) Freeman-Durden decomposition.

5. THE DATASET

Satellite scene: This analysis is demonstrated on a quad-pol fine mode Radarsat-2 image, which was collected north of Svalbard on April 12, 2011 (see Fig. 3). The image coincides with a good collection of ground truth data. The study area comprised first-year sea ice at different stages of development, plus open and refrozen leads.

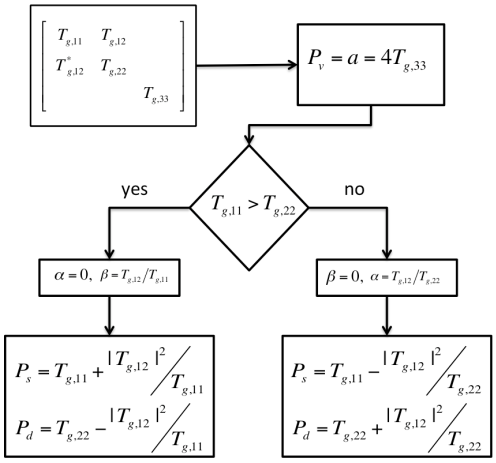

Figure 2. Freeman-Durden decomposition diagram.

Figure 3. Location of Radarsat-2 image, April 12, 2011. Red box north of Svalbard (center 81.1^oN 19.1^oE*).*

Ground truth: Ice thickness measurements over a large area were performed by a helicopter-borne electromagnetic induction sounder (EM-bird) [13]. These flights were also used to collect optical photos and roughness measurements with a laser altimeter. GPS trackers were placed on the ice to track the ice drift between the EM-Bird flight and satellite image acquisition. An Iridium Surface Velocity Profiler (SVP) buoy was deployed onto the ice on April 11. This buoy transmitted its position hourly, together with other parameters used for drift calculations. In addition, regular sea ice shipboard observations and photographs from the ship were collected. Fig.4 shows a Pauli image annotated with the original (red track) helicopter track. There is a time span of 1 h 46 min between the satellite image acquisition time and the final EM-bird measurements. The ice drift during this period is significant. Drift measurements from the GPS trackers and the buoy were utilized to correct for this drift. The drift corrected helicopter track is shown as the white lines in image Fig.4.

6. *RESULTS*

The segmentation result is shown in Fig.5. The image has been segmented into 7 classes. Sea ice experts interpreted the segmentation result aided by thickness measurements, optical photos and the Pauli image. Their interpretation is summarized in Table 1. Thickness measurements directly below the helicopter track clearly show that the red/blue classes are representing very thin ice, with a mean

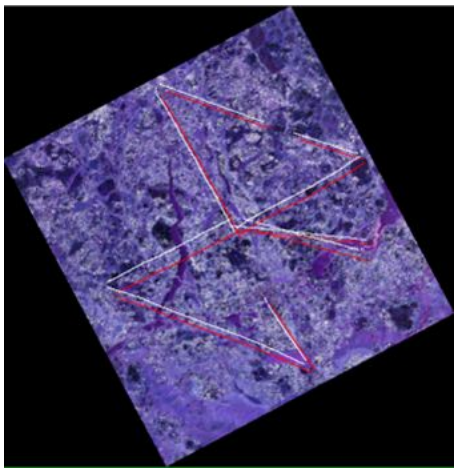

Figure 4. Geocoded Pauli image. The original helicopter track is shown in red and the ice drift corrected track in white.

thickness around 20cm. The green, black and yellow classes have an average thickness around 2 meters, the green and black being a bit thinner than the yellow. They all have thickness distributions with a distinct peak slightly below 2 meters, but with tails ranging up to 5 meters. The purple and cyan classes have approximately uniform thickness distributions, with mean thickness of about 1.75 meters.

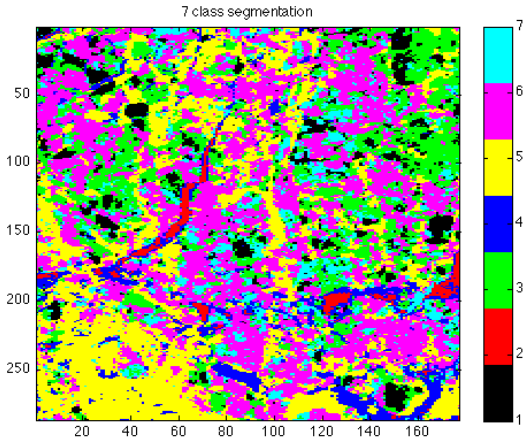

Figure 5. Automatic segmented image, showing 7 different classes.

Green/black/ yellow	first year ice, different stages of development
Purple/cyan	Young ice, thin first year ice (sometimes deformed and with snow cover)
Red/blue	Thin ice, open water, new ice, nilas, grey ice

Table 1. Class labels produced by sea ice experts

Fig.6 displays the relative contribution of surface scattering, double bounce scattering and volume scattering obtained by the NNED-Freeman-Durden decomposition. It can be seen that the dominant scattering mechanism is surface scattering. Double bounce scattering is almost absent, except for a tiny area in the lower right corner of the image. This area is thought to be characterized by ice broken up by the ship. However, we also see areas of significant volume scattering. Volume scattering is

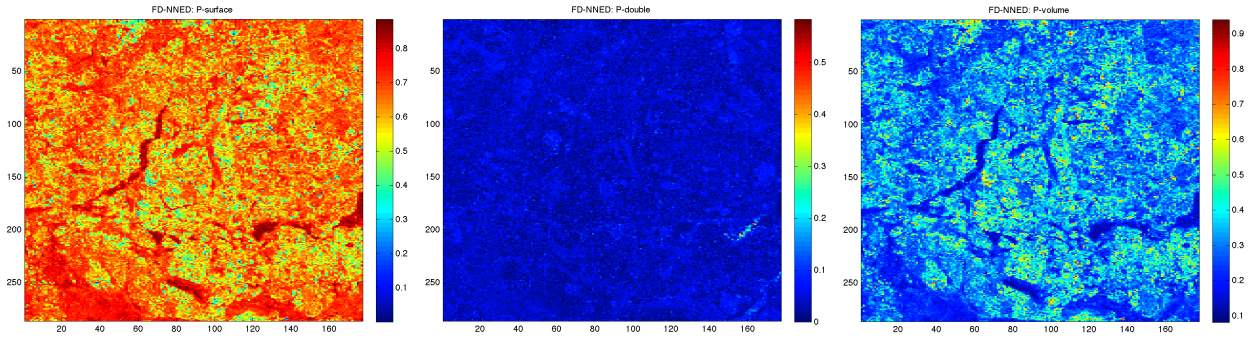

Figure 6. The relative contribution of surface (left), double bounce (middle) and volume scattering (right) as resulting from the NNED Freeman-Durden decomposition.

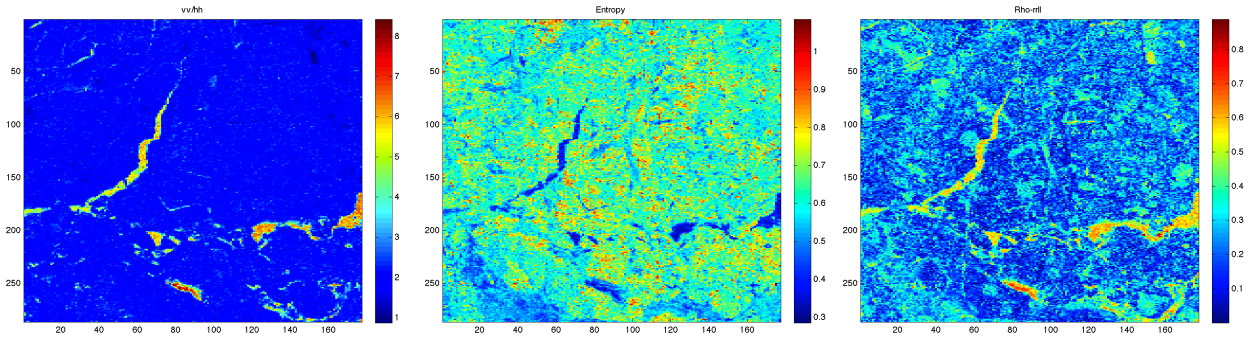

Figure 7. Left panel*: Co-polarization ratio.* Middle panel*: Polarimetric entropy.* Right panel*: Coherence between RR and LL circular polarization.*

here interpreted as originating from deformed ice. Fig.7 shows from left to right: The *co-polarization ratio*, *polarimetric entropy*, and *the coherence between RR and LL circular polarization*. The areas of high co-polarization ratio are leads, with the internal variations in the co-polarization ratio reflecting variations in the dielectric constant. This could be related to various amounts of newly frozen ice and open water. The same areas are characterized by high surface scattering, low entropy, and high like-circular coherence. All these observations points towards a relatively smooth surface dominated by Bragg-type scattering, as would be expected from open water and thin new-frozen ice.

By comparing the decomposition component images and polarimetric features with the segmented classes, we may conclude that the purple and cyan segments represent stages of deformed ice with significant volume scattering, where as the other colors are smoother ice, dominated by surface scattering. The red and blue classes are seen to correspond to very thin ice.

7. *SUMMARY AND CONCLUSIONS*

This paper presents an analysis of a Radarsat-2 PolSAR scene of Arctic sea ice, collected north of Svalbard in the winter 2011. The scene shows various stages of first year ice, plus some open and refrozen leads. The data set also comprised EM-bird thickness measurements and optical photos along a helicopter track covered by the SAR image. The analysis consisted of a segmentation step, which subdivided the scene into 7 classes based on statistical and polarimetric features. We applied a NNED Freeman-Durden decomposition on the data to decompose the image into dominant scattering mechanisms. We also tested some other well-known polarimetric parameters, the co-polarization ratio, the polarimetric entropy, and the coherence between LL and RR, with respect to their ability

to provide ice information. The analysis shows that the segmentation algorithm definitely enables segmentation of sea ice into proper segments, and some of these are easily identified as distinct ice types. The polarimetric parameters add information, which allows to distinguish between ice classes of different roughness. Our findings are similar to the conclusions made in [14], who claimed they were able classify three ice types by roughness.

ACKNOWLEDGMENTS

The authors acknowledge the sea ice experts at the Norwegian Polar Institute for input on ice segmentation. The research is funded by the Fram Centre project "Characterization of Arctic sea ice properties from remote sensing observations", the Norwegian Polar Institute's centre for Ice, Climate and Ecosystems, and RDA Troms.

REFERENCES

[1] W. Dierking, A. Carlstrom, and L. M. H. Ulander. The effect of inhomogeneous roughness on radar backscattering from slightly deformed sea ice. *IEEE Trans. Geosci. Remote Sens*, 35(1):147–159, 1997.

[2] S. V. Nghiem, R. Kwok, S. H. Yueh, and M. R. Drinkwater. Polarimetric signatures of sea ice: 1. theoretical model. *J. Geophys. Res.*, 100(C7):13681–13698, 1995.

[3] J. A. Kong. *Electromagnetic Wave Theory*. John Wiley, New York, 1986.

[4] J-S Lee and E. Pottier. *Polarimetric Radar Imaging, from basics to applications*. Taylor & Francis Group, 2009.

[5] Shane R. Cloude. *Polarisation: Applications in Remote Sensing*. Oxford University Press, Oxford, UK, 2010.

[6] W.-M. Boerner. Basic concepts in radar polarimetry. Technical report, UIC-ECE Communications, Sensing & Navigation Laboratory, Chicago, IL/USA, 2010.

[7] R. G. Valenzuela. Theories for the interaction of electromagnetic and oceanic waves - a review. *Boundary-Layer Meteorology*, 13(1-4):61–85, 1978.

[8] D. P.Winebrenner, L. D. Farmer, and I. R. Joughin. On the response of polarimetric synthetic aperture radar signatures at 24-cm wavelength to sea ice thickness in arctic leads. *Radio Science*, 30(2):373–402, 1995.

[9] H. Wakabayashi, T. Matsuoka, K. Nakamura, and F. Nishio. Polarimetric characteristics of sea ice in the sea of okhotsk observed by airborne l-band sar. *IEEE Trans. Geosci. Remote Sens*, 42(11):2412–2425, 2004.

[10] F. Mattia, F. T. Le Toan, J. C. Souyris, G. De Carolis, N. Floury, F. Posa, and G. Pasquariello. The effect of surface roughness on multifrequency polarimetric sar data. *IEEE Trans. Geosci. Remote Sens*, 35(4):954 – 966, 1997.

[11] A.P. Doulgeris and T. Eltoft. Scale mixture of gaussian modelling of polarimetric SAR data. *EURASIP J. Adv. Signal Processing*, pages 1–12, 2010.

[12] Anthony Freeman and Stephen L. Durden. A three-component scattering model for polarimetric SAR data. *IEEE Trans. Geosci. Remote Sens*, 36(3):963–973, May 1998.

[13] C. Haas, J. Lobach, S. Hendricks, L. Rabenstein, and A. Pfaffling. Helicopterborne measurements of sea ice thickness, using a small and lightweight, digital em system. *J. Appl. Geophys.*, 67(3):234–241, 2009.

[14] J.P.S.Gill and J.J. Yackel. Evaluation of C-band SAR polarimetric parameters for discriminating of first-year sea ice types. *Can. J. Remote Sens.*, 38(3):306–323, 2012.